ADVANCED OPTICAL MATERIALS
www.advopticalmat.de



# Ultrabroadband Plasmonic Absorber for Terahertz Waves

*Yong Zhi Cheng, Withawat Withayachumnankul,* Aditi Upadhyay, Daniel Headland, Yan Nie, Rong Zhou Gong, Madhu Bhaskaran, Sharath Sriram,* and Derek Abbott*

**Perfect absorbers that exhibit broadband absorption of terahertz radiation are promising for applications in imaging and detection due to enhanced contrast and sensitivity in this relatively untapped frequency regime. Here, terahertz plasmonics is used to demonstrate near-unity absorption across a broad spectral range. The absorber comprises a planar array of cross-shaped structures defined by surface etching of doped silicon. Absorbance of over 90% is observed numerically with a relative bandwidth of 90% from 0.67 to 1.78 THz, in reasonable agreement with experimental observation. This ultrabroadband absorption is attributed to two resonance modes supported by plasmonic cavities that are defined by the etched cross structure. This terahertz absorber is single-layered, polarization-insensitive, and exhibits consistent performance across a wide range of incidence angles. The plasmonic-based approach for enhancing absorption is a potential precursor to the realization of efficient bolometric imaging and communications at terahertz frequencies.**

## 1. Introduction

Terahertz (or T-ray) radiation typically refers to the electromagnetic (EM) spectrum spanning 0.1–10 THz, and is a largely untapped frequency regime between microwave and optical frequencies. A number of unique characteristics make terahertz radiation suited to imaging for security and material analysis, medical diagnostics, chemical and biological sensing, and ultrahigh data rate short-path wireless communications.[1–4] While the last two decades have seen increased research efforts and understanding of terahertz phenomena, high-performance terahertz devices are still lacking. An example is the need for a perfect absorber of terahertz waves, which has applications in high-resolution terahertz imaging and detection for security and biomedicine.

By definition, perfect absorbers can absorb EM waves with near-unity absorbance, which are promising for applications in terahertz imaging and detection via enhanced contrast and sensitivity. Metamaterials are candidates for creating perfect absorbers owing to the possibility of tailoring the response of the structure with great flexibility.[5,6] Landy et al.[7] first demonstrated the perfect metamaterial absorber concept in the microwave range, and since then great interest in EM absorbers has extended toward optical frequencies in recent years.[8–22] Metamaterial absorbers typically consist of two coupled metallic layers separated by a dielectric spacer to create electric and magnetic responses for impedance matching with free space.[23] The electric response can be obtained from excitation of the top metal layer readily coupled to an external electric field, while the magnetic response is provided by pairing the top layer with a metal ground plane or metal wire for an external magnetic field. In the microwave and terahertz regions, these metamaterial absorbers obtain high absorption through dielectric loss and impedance matching at resonance.[23] The absorption frequency range and amplitude can be tuned by adjusting the shape, size, thickness, and properties of the metallic structure and dielectric spacer. Due to the nature of resonance response, these metamaterial absorbers usually exhibit narrowband absorption that has advantages in applications such as filtering, sensing, and modulation.[24] Broadband perfect absorbers are desirable for other applications such as high-efficiency signal detection and communications. This has necessitated significant research effort toward extending the absorption bandwidth. A straightforward approach is to cluster multiple resonating structures with different sizes in each unit cell to create a number of absorption bands.[9,22]

Graphene has been introduced to construct broadband terahertz absorbers due to its exceptional properties, such as optical transparency, flexibility, and tunability.[25–27] However, the structure is demanding in terms of cost and complexity. Another alternative promising material for terahertz absorption is a moderately doped semiconductor, which can be readily fabricated using conventional micro-fabrication techniques. At terahertz frequencies, doped semiconductors have desirable conductive loss, enabling them to sustain surface plasmon polaritons (SPPs) and correspondingly localized surface plasmon resonances (LSPRs) via periodic structures.[28–30] Recently, we have demonstrated that doped silicon can be engineered to attain highly

Y. Z. Cheng, Dr. W. Withayachumnankul
D. Headland, Prof. D. Abbott
School of Electrical & Electronic Engineering
The University of Adelaide
Adelaide, South Australia 5005, Australia
E-mail: withawat@eleceng.adelaide.edu.au
Y. Z. Cheng, Prof. Y. Nie, Prof. R. Z. Gong
School of Optical and Electronic Information
Huazhong University of Science and Technology
Wuhan 430074, China
Dr. W. Withayachumnankul, A. Upadhyay, Dr. M. Bhaskaran, Dr. S. Sriram
Functional Materials and Microsystems Research Group
RMIT University
Melbourne, Victoria 3001, Australia
E-mail: sharath.sriram@rmit.edu.au

**DOI: 10.1002/adom.201400368**

efficient narrowband perfect absorption with a plasmonic coaxial mode.[31] In this work, we show that distinctive plasmonic modes in silicon-based cavities can serve to greatly enhance the absorption bandwidth for ultrabroadband operation. Our single-layered structure is more attractive than prior broadband multilayered absorbers in terms of fabrication simplicity, cost, and allows for possible integration into silicon-based systems.

## 2. Design

The plasmonic absorber is in the form of a 2D array of cross structures etched into a doped silicon substrate. **Figure 1**a illustrates an optimal design, together with the field directions. Either of the two dotted areas in the 2D array can be regarded as a unit cell of the plasmonic absorber. Particularly, the unit cell defined by the etched middle region, as shown by the red-dotted box, can be seen as a resonant cavity, which can support different LSPRs in the terahertz frequency range. The depth of the cavity, $t_b$, is 65 μm, which is comparable to a quarter of the free-space wavelength at 1 THz. To obtain strong LSPRs for this cross structure, a phosphorous-doped (n-type) silicon wafer of (100) orientation is utilized. Specifically, the material resistivity of this wafer is between 0.02 and 0.05 Ω cm.[30] To study its efficiency and gain insight into the mechanism of the enhanced absorption, finite element method (FEM) simulations are performed by using the frequency domain solver in CST Microwave Studio for the unit cell structure with a Drude model for the silicon.

Microfabrication as a combination of photolithography and plasma-assisted DRIE was undertaken to realize the structures in Figure 1a. Samples 35 × 35 mm$^2$ in area were produced, containing 30 625 identical cross structures. Figure 1b,c presents scanning electron images of the fabricated unit-cell structure and the cross array, respectively. Relatively smooth and straight

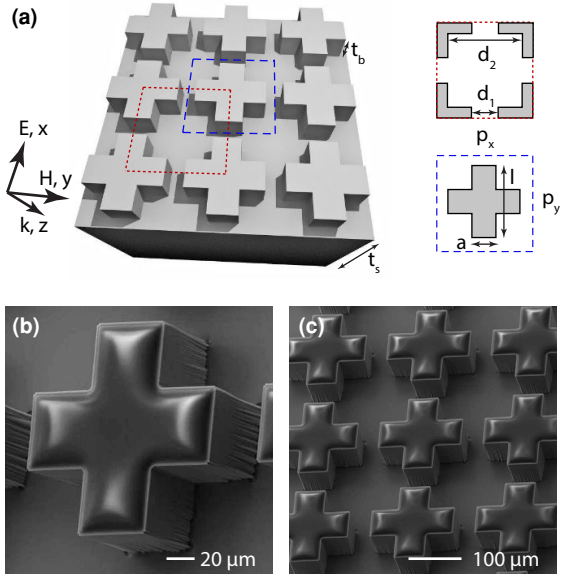


**Figure 1.** The plasmonic absorber. a) Schematic of a 2D array carved from a doped silicon substrate. The geometric parameters are: $p_x = p_y = 200$ μm, $t_b = 65$ μm, $a = 60$ μm, $l = 160$ μm, and $t_s = 200$ μm. b,c) Scanning electron images of the fabricated cross structure viewed at a 35° from the normal.

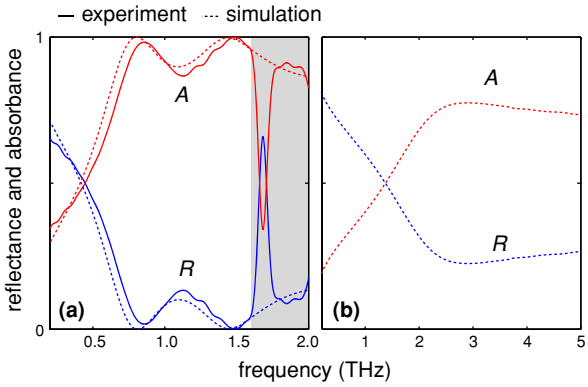


**Figure 2.** Numerically and experimentally resolved spectra. a) Reflectance $R(\omega)$ and absorbance $A(\omega)$ for the 2D cross array absorber. b) Reflectance $R(\omega)$ and absorbance $A(\omega)$ for the bare, doped silicon substrate. The shaded area marks the limit of the system dynamic range

sidewalls of the crosses are apparent in the images. Following microfabrication, reflection-mode terahertz time-domain spectroscopy (THz-TDS) is performed on the sample at normal incidence.

## 3. Results and Discussion

**Figure 2**a shows the results for the designed and fabricated plasmonic absorber. It can be seen that the numerical and experimental results are in good agreement, with a slight blue shift in the spectral response observed in the experiment. A small deviation between the numerical and experimental results is caused by tolerances in fabrication and measurement and the limit of the system dynamic range at higher frequencies. From the measurement, the reflectance reaches minima of 1.78% and 0.15% at the frequencies of 0.86 and 1.49 THz. These reflectance minima correspond to the absorbance of 98.22% and 99.85%, respectively. The simulated absorbance is more than 90% from 0.67 to 1.78 THz, and hence, the relative bandwidth is 90%. As for the bare silicon in Figure 2b, the absorbance determined from the simulated reflectance increases with an increase of the frequency and up to a maximal value of 78% at around 2.7 THz, where the material becomes dielectric. Hence, it can be deduced that the two absorption peaks observed in the absorber are associated with two plasmonic resonances, which can be excited by incident linearly polarized terahertz waves.

The current densities and field distributions on the absorber are shown in **Figure 3**, for both of the resonances at 0.80 and 1.44 THz. From Figure 3a,b, we find that the current density for the lower resonance at 0.80 THz is mainly on the top and bottom arms, while that for the higher at 1.44 THz concentrates on the left and right arms. The current distribution at the lower frequency suggests that the cross structure does not resonate by itself as in the case of metallic resonators, for which the current is relatively strong in the middle region.[32] From the field distributions in Figure 3c,d, it is clear that at the lower resonance the electric field is localized in the small cavity formed between the top and bottom arms, while at the higher resonance the field concentrates in the large square cavity formed by the four adjacent resonators. Further observation of the field distributions (not shown) suggest that the lower and higher resonances originate



Adv. Optical Mater. 2014,
DOI: 10.1002/adom.201400368

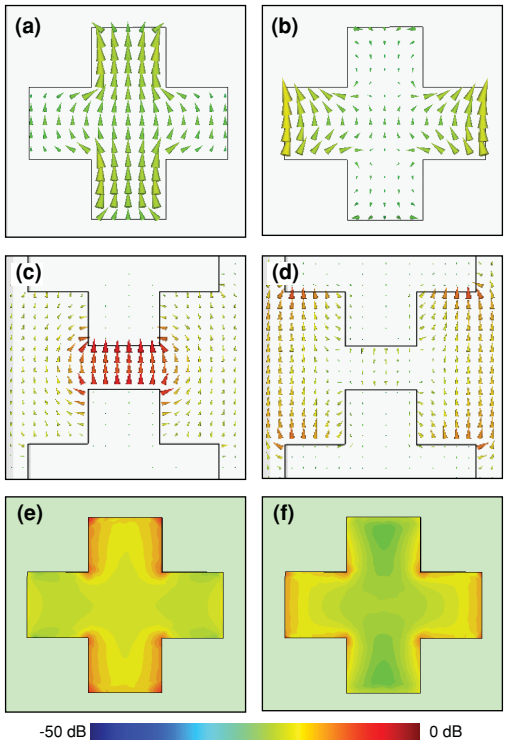


**Figure 3.** Field distributions of the plasmonic absorber at resonance frequencies. Results for both resonance frequencies are presented: 0.80 THz (left column) and 1.44 THz (right column). Shown are the a,b) Current density distributions on the cross structure, c,d) the instantaneous electric fields between the adjacent cross structures, and e,f) power loss density distributions.

from cavity modes in the small and large cavities, respectively. These cavity modes are responsible by terahertz SPPs propagating along the cavity walls in the $z$ direction, and coincide with the decay lengths of SPPs perpendicular to the walls. At 1 THz, the decay length into the silicon resolved analytically and numerically is merely around 12 μm, much shallower than the silicon wall thickness. On the other hand, the decay length into air is as far as 330 μm, spanning the cavity air gaps $d_1 = 40$ μm and $d_2 = 140$ μm to establish SPP-coupled modes there.

The resonance frequencies of the observed cavity modes can be analytically determined from the dispersion behavior of equivalent plasmonic waveguides made of the doped silicon. For the lower resonance, the small cavity formed between the top and bottom arms of the adjacent crosses can be considered by using a plasmonic parallel-plate waveguide, i.e., a conductor–insulator–conductor heterostructure, with a separation of the plates of $d_1 = 40$ μm. Since the cavity is excited by linearly polarized incident waves, the mode of coupled SPPs in this waveguide is the odd mode with the $E_x(x)$ component being even function, and can be explained by:[28]

$$\tanh\left(k_0 \frac{d}{2}\right) = -\frac{k_m \varepsilon_0}{k_0 \varepsilon_m} \tag{1}$$

where $k_m^2 = \beta^2 - k_0^2 \varepsilon_m$ and $k_0^2 = \beta^2 - k_0^2 \varepsilon_0$. In this expression, $\varepsilon_m$ and $\varepsilon_0$ represent the relative permittivity of the doped silicon and free space, respectively; $k_0 = \omega/c$ is the free-space wave vector; and $\beta$ is the SPP-wave vector along the propagation axis. For the higher resonance, the large square cavity formed by the four adjacent resonators can be approximately modeled by a rectangular plasmonic waveguide[33] with a width and height equal to $d_2 = 140$ μm. The mode of interest in this waveguide is a $TE_{10}$-like mode, namely a SPP even mode, which can be characterized by the even $E_x(x)$ component.

**Figure 4** shows the dispersion curves for both the parallel-plate and rectangular plasmonic waveguides with different dimensions. It can be seen that the waveguide dimensions can strongly influence the SPP wavenumbers. Additionally, owing to the field confinement, the wavenumber of the rectangular plasmonic waveguides is greater than the $TE_{10}$ wavenumber in the equivalent PEC waveguide. Likewise, the wavenumber of the parallel-plate plasmonic waveguides lie to the right of the light line (TEM wave). The condition for the plasmonic resonance can be approximated to

$$\beta_N = (2N + m)\pi / 2t_b \tag{2}$$

where $\beta_N$ is the SPP wavenumber inside the cavity for the $N$th-order resonance ($N = 0, 1, 2,...$), $t_b$ is the cavity depth, and $m = 0.9$ for the plasmonic boundary.[30] By using Equation (2), together with the dispersion curves of the waveguides, we can estimate the resonance frequencies of the plasmonic cavity. From the resonance condition, the cavity with the depth $t_b$ of 65 μm is expected to exhibit the fundamental resonance $N = 0$ at the wavenumber of $\beta_0 = 2.17 \times 10^4$ rad m$^{-1}$. Thus, as depicted in Figure 4, the plasmonic resonance frequencies are estimated to be around 0.89 and 1.36 THz for this cavity, in reasonable agreement with 0.80 and 1.44 THz from the simulation, and 0.86 and 1.49 THz from the experiment, respectively. The inaccuracy of the analytical results is likely due to the fringing fields at the top and side openings of the cavities, not accounted for in the analysis.

From the dispersion diagram and resonance condition, it can be expected that the fundamental resonances and the absorption band of this plasmonic absorber can be readily tuned by changing the cavity depth $t_b$ and the gap sizes $d_1$ and $d_2$. More

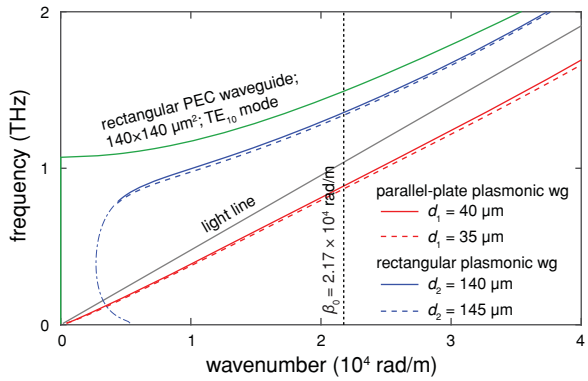


**Figure 4.** Dispersion diagram of the coupled surface plasmon polaritons in the equivalent parallel-plate and rectangular plasmonic waveguides. The vertical-dotted line indicates the wavenumber $\beta_0$ where the fundamental resonance is expected for cavity with a depth of 65 μm. The thin dash-dotted line section for the rectangular plasmonic waveguides indicates the region where the loss is larger than the propagation constant, i.e., Im($\beta$) > Re($\beta$).

specifically, by increasing the cavity depth $t_b$, the two plasmonic resonances will be shifted to lower frequencies, and from the dispersion diagram in Figure 4, the relative absorption bandwidth will be slightly increased. In addition, by increasing the length $l$ of the cross structure, the small gap width $d_1$ will be reduced, resulting in a redshift of the lower resonance. Likewise, decreasing the width $a$ of the cross increases the gap width $d_2$ and effectively redshifts the higher resonance. The effects are further confirmed by numerical simulation (not shown). Although the bandwidth can be increased by fine tuning the lower and higher resonances, the high level of absorption between the two resonances will be compromised.

It should be noted that the carrier concentration in silicon affects the resonances and the observed power loss behavior. By decreasing the carrier concentration, the silicon will become a lossy dielectric, and no longer support LSPRs. As a result, the absorption will be decreased significantly, and the power loss density will be evenly distributed across the unit cell. On the other hand, increasing the carrier concentration will decrease the field penetration into silicon. In this case, the geometry of the structure has to be modified to maintain the resonances, while the dissipation loss and the resonance $Q$ factor will be significantly reduced.

We further investigate the origin of the loss in our design by studying the power loss density distributions. Confirmed in Figure 3e,f, the majority of energy dissipation originates from the Ohmic loss inside the silicon walls through the strong LSPRs. Corresponding to the current density distributions, the power loss density for the lower resonance is mainly concentrated inside the top and bottom branches of the cross, while the one of the higher resonance is mainly concentrated on the left and right arms. The Ohmic loss origin of this plasmonic absorber stands in contrast with the losses due to the interlayer dielectric in conventional terahertz metamaterials absorbers composed of the metal/dielectric/metal structure.[23]

Since the structure is fourfold symmetric, it can be expected that the absorber is polarization insensitive for terahertz waves of normal incidence. We further characterized the angle-dependent response of the designed plasmonic absorber. **Figure 5** presents the absorbance as a function of frequency and angle of incidence. It is clear that the proposed absorber can operate over a wide range of incidence angles for both the TE and TM polarizations. For the TE wave at oblique incidence angle in Figure 5a, the broadband absorption performance is maintained up to 45°. Beyond 45°, the absorption is degraded because the phase front of the electric field makes a large angle with the surface in the $H$ plane, resulting in a field imbalance in the cavity. For the case of TM polarization in Figure 5b, the absorbance is minimally affected with an increasing incidence angle, since the phase front of the electric field is always parallel to the surface in the $H$ plane. It is noteworthy that Figure 5 also reveals additional resonance modes associated with the cavities and diffraction orders associated with the structural periodicity.

We now discuss the benefits and potential applications of the plasmonic absorbers based on the 2D cross array. First, the fabrication technology to create this structure is well established, and this aspect is also readily integrated into silicon-based optical systems. Compared with existing terahertz absorbers,[23] our device is ultrabroadband, is also polarization insensitive, and can sustain absorption at large incidence angles.

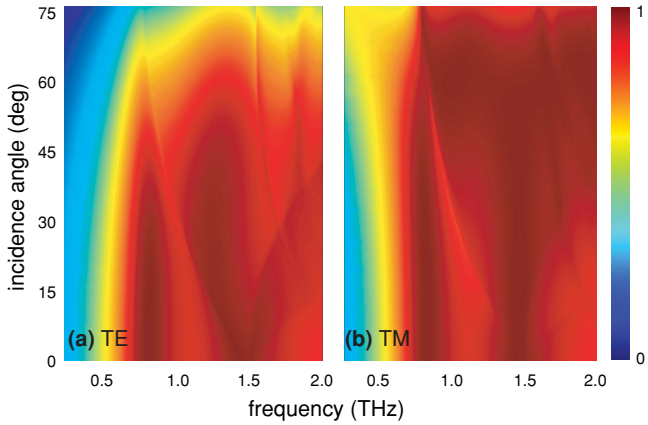


**Figure 5.** Absorption performance as a function of incidence angle $\theta$. a) TE polarization. b) TM polarization. The incident angle is varied in 1° steps from 0° to 75°.

Furthermore, the plasmonic resonances are readily tunable, since the terahertz properties of the silicon strongly depend on the free-carrier concentration and mobility that can be controlled by optical pumping.[34] These benefits for our plasmonic absorber are ideal for constructing focal plane array detectors allowing room-temperature high-resolution imaging at terahertz frequencies range. In addition, due to its ability to capture nearly the entire incident EM energy at terahertz frequencies, the plasmonic absorber can serve as a useful component in terahertz communications for suppressing multipath reflections.

## 4. Conclusion

We have designed and experimentally validated a plasmonic perfect absorber for terahertz waves. We achieve an experimental absorbance of 98.22% and 99.85% at resonance frequencies of 0.86–1.49 THz, and over 90% absorbance from 0.67 to 1.78 THz, which corresponds to a relative bandwidth of 90%. Overall, the results demonstrate that our design yields broadband near-perfect absorption over a wide range of incidence angles for both TE and TM waves. The bandwidth can be extended further with alternative designs to accommodate mode resonance modes. Our plasmonic absorber can potentially be implemented in many applications, such as in bolometric imaging and terahertz communications.

## 5. Numerical and Experimental Section

*FEM Simulations*: Full wave electromagnetic simulations are performed using the frequency domain solver in CST Microwave Studio based on a finite element method (FEM). In the simulation, the dielectric properties of the silicon wafer are described via the Drude model as shown in the literature:[35]

$$\varepsilon_m = \varepsilon_c - \frac{\omega_p^2}{\omega^2 + i\gamma\omega} \quad (3)$$

where the plasma frequency $\omega_p$ is $2\pi \times 7.87$ THz; the collision frequency $\gamma$ is $2\pi \times 1.78$ THz, and the permittivity at the high-frequency limit $\varepsilon_c$



*Adv. Optical Mater.* **2014**,
DOI: 10.1002/adom.201400368

is 11.68. These values are determined from the carrier concentration and mobility, which are obtained through terahertz reflection spectroscopy.[30,35] In the simulation, the unit cell boundary condition is applied for the transverse boundaries to replicate an infinite planar array of the cross structures. A plane-wave excitation with a linear polarization is incident on the unit cell along the $+z$ direction, and the transmission and reflection are monitored. The frequency-dependent transmittance $T(\omega) = |S_{21}(\omega)|^2$ and reflectance $R(\omega) = |S_{11}(\omega)|^2$ obtained from the simulation are used to calculate the absorbance according to $A(\omega) = 1 - T(\omega) - R(\omega)$. Since the silicon substrate is thick enough to suppress field transmission to the other side, the transmittance is negligible across the entire frequency range for the present design. Thus, both the simulated and measured absorbance can be calculated using $A(\omega) = 1 - R(\omega)$.

*Fabrication*: We fabricate the plasmonic absorber by using conventional microfabrication techniques involving photolithography and deep-reactive ion etching (DRIE).[30,31] Note that DRIE was performed using the Bosch process, where a mixture of SF6 (to etch silicon) and C4F8 (to passivate sidewalls to enable deep etching) gas was alternatively permitted into the high vacuum chamber and ionized by applying RF power. The etch rate of the silicon wafer using the Bosch DRIE process was approximately 0.4 μm per cycle, with process timed to etch 65-μm deep trenches into the doped silicon wafer. The quality, including the depth and smoothness, of the fabricated structure is then examined using a FEI Nova field emission gun SEM.

*Measurement*: The absorber characterization was carried out by the use of reflection-mode THz-TDS at normal incidence. The generated linearly polarized terahertz beam propagates through a beam splitter and is then focused by an off-axis parabolic mirror onto the sample at normal incidence. The reflected beam from the sample is then collected by the same mirror and back to the beam splitter that partially reflects the energy into the photoconductive antenna (PCA). A gold-coated mirror replaces the sample for reference measurement. The total scanning duration time is 55 ps and is digitized with a step size of 0.067 ps.

## Acknowledgements

W.W. and D.A. acknowledge funding via the Australian Research Council (ARC) Discovery Project DP120100200. M.B. and S.S. acknowledge ARC Postdoctoral Fellowships DP1092717 and DP110100262, respectively. S.S. acknowledges partial support from Victoria and AFAS-Vic Fellowships. Y.Z.C. and Y.N. acknowledge the National Natural Science Foundation of China (No. 51207060) and the foundation for Chinese Scholarship Council (No. 201306160039). The assistance of Henry Ho, Philipp Gutruf, Charan Shah, and Dan Smith is also gratefully acknowledged. Technical support from staff at the RMIT Microscopy and Microanalysis Facility and the Melbourne Centre for Nanofabrication is acknowledged, along with funding from the National Collaborative Research Infrastructure Scheme.

Received: August 20, 2014
Revised: October 6, 2014
Published online:

[1] B. Ferguson, X. C. Zhang, *Nat. Mater.* **2002**, *1*, 26.
[2] W. Withayachumnankul, G. M. Png, X. Yin, S. Atakaramians, I. Jones, H. Lin, B. S. Y. Ung, J. B. Balakrishnan, W. H. Ng, B. Ferguson, S. P. Mickan, B. M. Fischer, D. Abbott, *Proc. IEEE* **2007**, *95*, 1528.
[3] M. Tonouchi, *Nat. Photonics* **2007**, *1*, 97.
[4] P. U. Jepsen, D. G. Cooke, M. Koch, *Laser Photonics Rev.* **2011**, *5*, 124.
[5] D. Shrekenhamer, W. Xu, S. Venkatesh, D. Schurig, S. Sonkusale, W. J. Padilla, *Phys. Rev. Lett.* **2012**, *109*, 177401.
[6] L. Luo, I. Chatzakis, J. Wang, F. B. P. Niesler, M. Wegener, T. Koschny, C. M. Soukoulis, *Nat. Commun.* **2014**, *5*, 3055.
[7] N. I. Landy, S. Sajuyigbe, J. J. Mock, D. R. Smith, W. J. Padilla, *Phys. Rev. Lett.* **2008**, *100*, 207402.
[8] N. I. Landy, C. M. Bingham, T. Tyler, N. Jokerst, D. R. Smith, W. J. Padilla, *Phys. Rev. B* **2009**, *79*, 125104.
[9] Q. Y. Wen, W. Z. Hua, S. X. Yun, Y. Q. Hu, L. Y. Li, *Appl. Phys. Lett.* **2009**, *95*, 241111.
[10] Y. Q. Ye, Y. Jin, S. He, *J. Opt. Soc. Am. B* **2010**, *27*, 498.
[11] X. Liu, T. Starr, A. F. Starr, W. J. Padilla, *Phys. Rev. Lett.* **2010**, *104*, 207403.
[12] N. Liu, M. Mesch, T. Weiss, M. Hentschel, H. Giessen, *Nano. Lett.* **2010**, *10*, 2342.
[13] K. Aydin, V. E. Ferry, R. M. Briggs, H. A. Atwater, *Nat. Commun.* **2011**, *2*, 517.
[14] K. B. Alici, A. B. Turhan, C. M. Soukoulis, E. Ozbay, *Opt. Express* **2011**, *18*, 14260.
[15] S. Chen, H. Cheng, H. Yang, J. Li, X. Duan, C. Gu, J. Tian, *Appl. Phys. Lett.* **2011**, *99*, 253104.
[16] Y. Cui, Kin H. Fung, J. Xu, H. Ma, Y. Jin, S. He, N. X. Fang, *Nano Lett.* **2012**, *12*, 1443.
[17] Q. Liang, T. Wang, L. Zu, Q. Sun, Y. Fu, W. Yu, *Adv. Optical Mater.* **2013**, *1*, 43.
[18] J. Dai, F. Ye, Y. Chen, M. Muhammed, M. Qiu, M. Yan, *Opt. Express* **2013**, *21*, 6697.
[19] T. Cao, C. Simpson, E. Robert, L. Zhang, M. J. Cryan, *Sci. Rep.* **2014**, *4*, 3955.
[20] Y. Z. Cheng, H. Yang, Z. Z. Cheng, N. Wu, *Appl. Phys. A* **2011**, *102*, 99.
[21] Y. Ma, Q. Chen, J. Grant, S. C. Saha, A. Khalid, D. R. S. Cumming, *Opt. Lett.* **2011**, *36*, 945.
[22] L. Huang, D. R. Chowdhury, S. Ramani, M. T. Reiten, S. N. Luo, A. J. Taylor, H. T. Chen, *Opt. Lett.* **2012**, *37*, 154.
[23] C. M. Watts, X. Liu, W. J. Padilla, *Adv. Mater.* **2012**, *24*, 98.
[24] C. M. Watts, D. Shrekenhamer, J. Montoya, G. Lipworth, J. Hunt, T. Sleasman, S. Krishna, D. R. Smith, W. J. Padilla, *Nat. Photonics* **2014**, *8*, 605.
[25] S. He, T. Chen, *IEEE Trans. Terahertz Sci. Technol.* **2013**, *3*, 757.
[26] M. Amin, M. Farhat, H. Bagcı, *Opt. Express* **2013**, *21*, 29938.
[27] A. Andryieuski, L. Andrei, *Opt. Express* **2013**, *21*, 9144.
[28] S. A. Maier, *Plasmonics: Fundamentals and Applications*, Springer, UK, **2007**.
[29] V. Giannini, A. Berrier, S. A. Maier, J. A. Sánchez-Gil, J. G. Rivas, *Opt. Express* **2010**, *18*, 2797.
[30] W. Withayachumnankul, C. M. Shah, C. Fumeaux, K. Kaltenecker, M. Walther, B. M. Fischer, D. Abbott, M. Bhaskaran, S. Sriram, *Adv. Opt. Mat.* **2013**, *1*, 443.
[31] W. Withayachumnankul, C. M. Shah, C. Fumeaux, B. S.-Y. Ung, W. J. Padilla, M. Bhaskaran, D. Abbott, S. Sriram, *ACS Photonics* **2014**, *1*, 625.
[32] W. Withayachumnankul, D. Abbott, *IEEE Photonics J.* **2009**, *1*, 99.
[33] F. Kong, B.-I. Wu, H. Chen, J. A. Kong, *Opt. Express* **2007**, *15*, 12331.
[34] A. Berrier, R. Ulbricht, M. Bonn, J. Gomez Rivas, *Opt. Express* **2010**, *18*, 23226.
[35] D. Hashimshony, I. Geltner, G. Cohen, Y. Avitzur, A. Zigler, C. Smith, *J. Appl. Phys.* **2001**, *90*, 5778.